

Supplementary Information

Polyethenetetrathiolate or Polytetrathiooxalate? Improved synthesis, a comparative analysis of a prominent thermoelectric polymer and implications to charge transport mechanism.

Roman Tkachov,^{*ab} Lukas Stepien,^a Robert Grafe,^a Olga Guskova,^c Anton Kiriya,^c

Frank Simon,^c Heiko Reith,^d Kornelius Nielsch,^d Gabi Schierner,^d Deepa Kasinathan^e and Christoph Leyens^{ab}

Table of Contents

A) Thermoelectric properties

B) Simulation Data

C) XPS data

D) Thermogravimetric and elemental analysis

E) Scheme of tentative polymerization mechanism

A) Thermoelectric properties

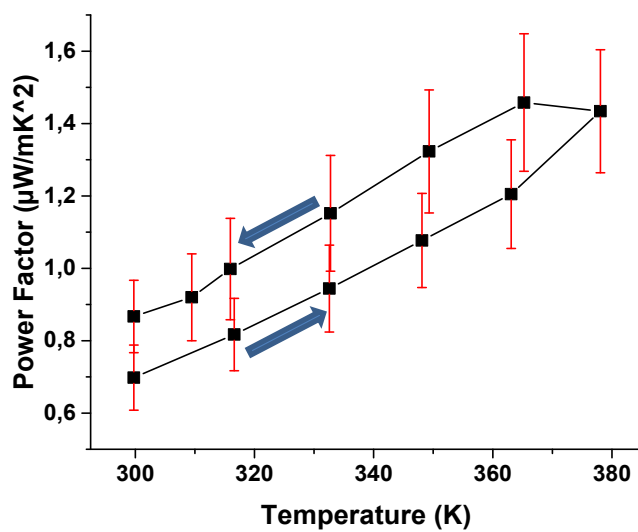
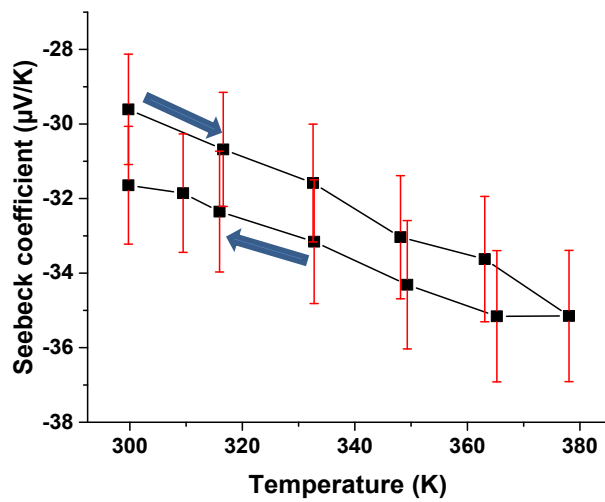
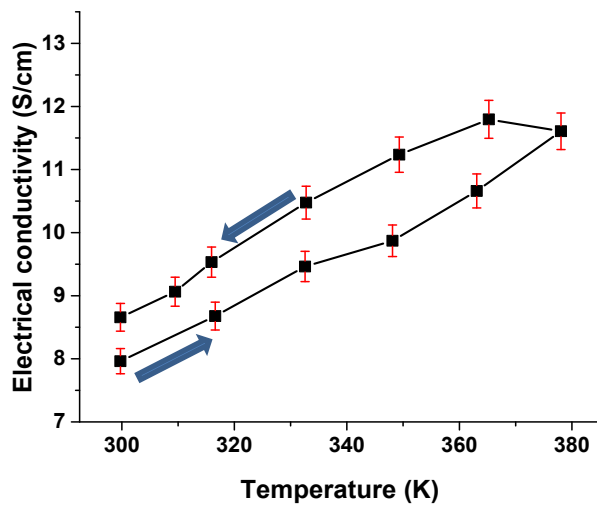


Fig. SA1. The electrical conductivity, the Seebeck coefficient and the power factor of poly[K_x(Ni-ett)] (P1_{methanol}), measured on compressed pellets at 300-380 K. (The arrows show the direction of the measurement sequence).

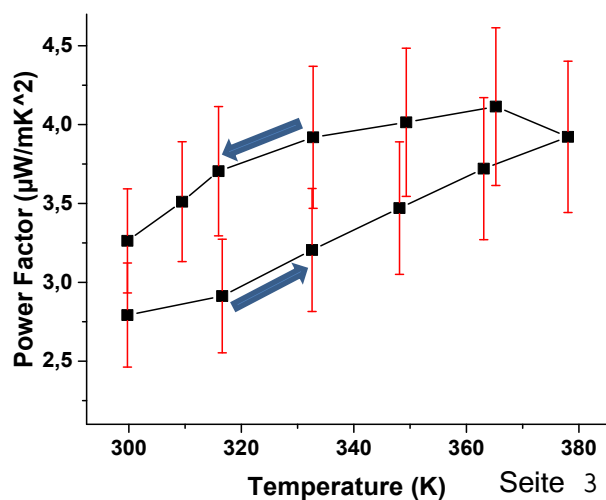
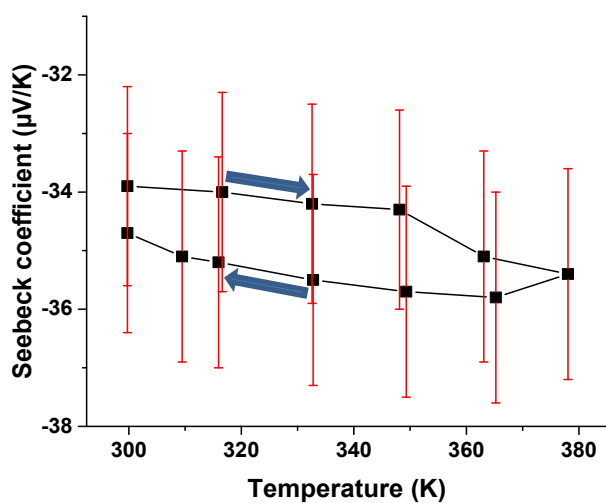
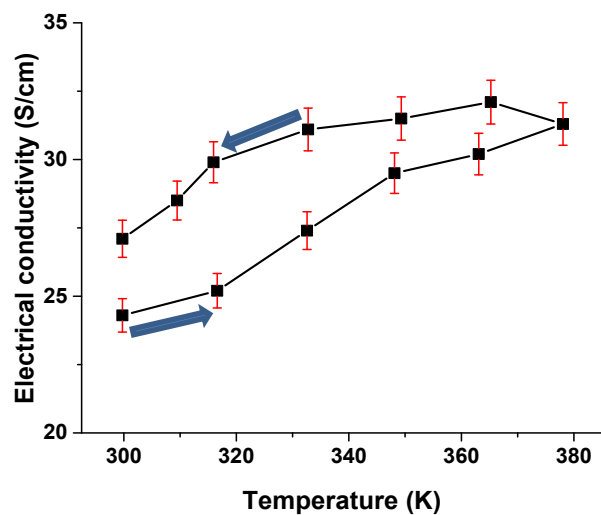


Fig. SA2. The electrical conductivity, the Seebeck coefficient and the power factor of poly[K_x(Ni-ett)] (P1), measured on compressed pellets at 300-380 K. (The arrows show the direction of the measurement sequence).

Density, g/cm³	σ (S cm⁻¹)
2.0235	2.35
2.0444	2.69
2.0864	2.95

Table SA1. Dependence of the electrical conductivity (σ) of one batch Poly[K_x(Ni-ett)] on the pellet density (300 K). The powders were pressed under different pressure to form the pellets of various densities. The electrical conductivity of high-density materials is higher than the lower-density materials.

Density, g/cm³	σ (S cm⁻¹)
2.0106	29.79
2.0278	30.50
2.1062	34.63

Table SA2. Dependence of the electrical conductivity (σ) of one batch Poly[Ni-tto] on the pellet density (300 K). The powders were pressed under different pressure to form the pellets of various densities. The electrical conductivity of high-density materials is higher than the lower-density materials.

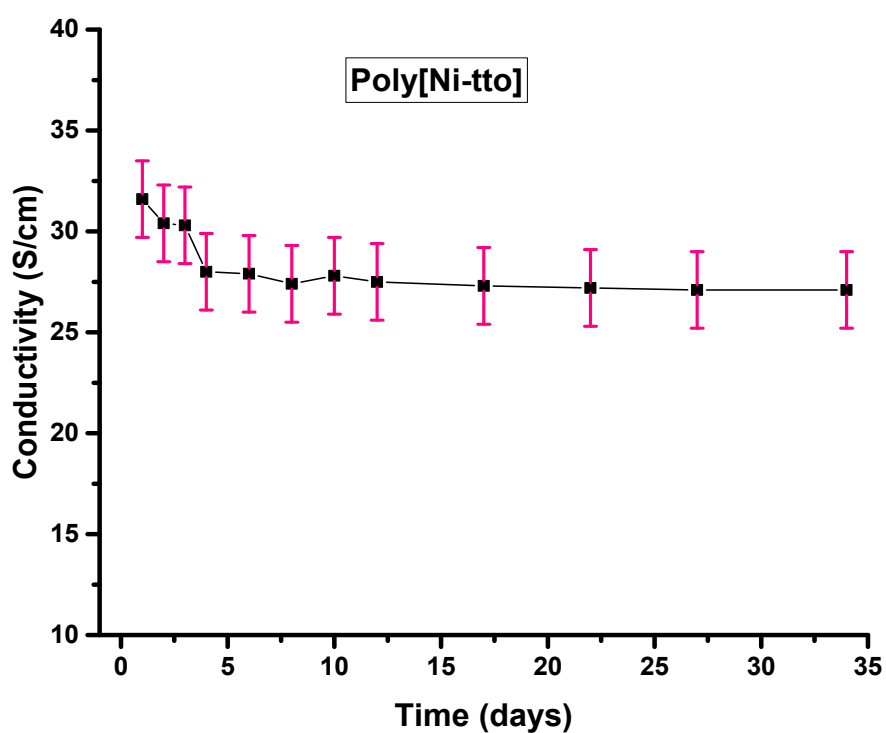
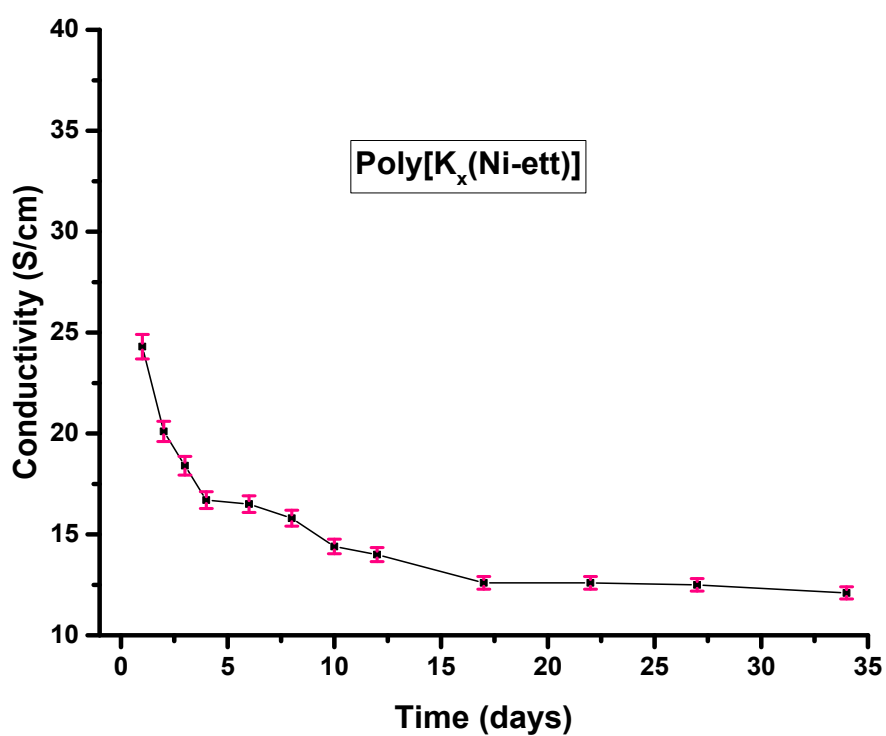


Fig. SA3. Deterioration of electrical conductivity of poly[K_x(Ni-ett)] and poly[Ni-tto] under ambient atmosphere over time.

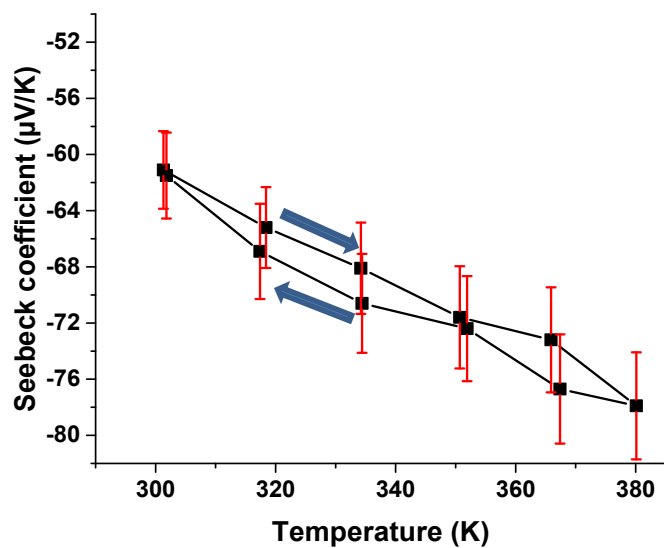
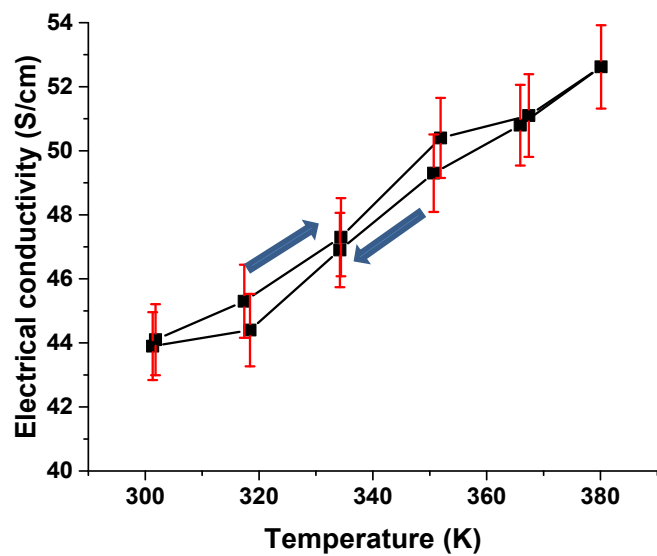


Fig. SA4. The temperature depended electrical conductivity and the Seebeck coefficient of poly[Ni-tto] (P3, compressed pellets), that was previously annealed at 110°C during 1 hour. (The arrows show the direction of the measurement sequence).

The figure **SA5** shows the reproducibility of the thermoelectric characteristics for poly[Ni-tto]. Extreme values differ by 1.7 and 1.4 times for electrical conductivity and Seebeck coefficient respectively. To compare: the scatter of poly[K_x(Ni-ett)] electrical conductivity values in accordance with the literature data is more than one order of magnitude (see Introduction of the main part).

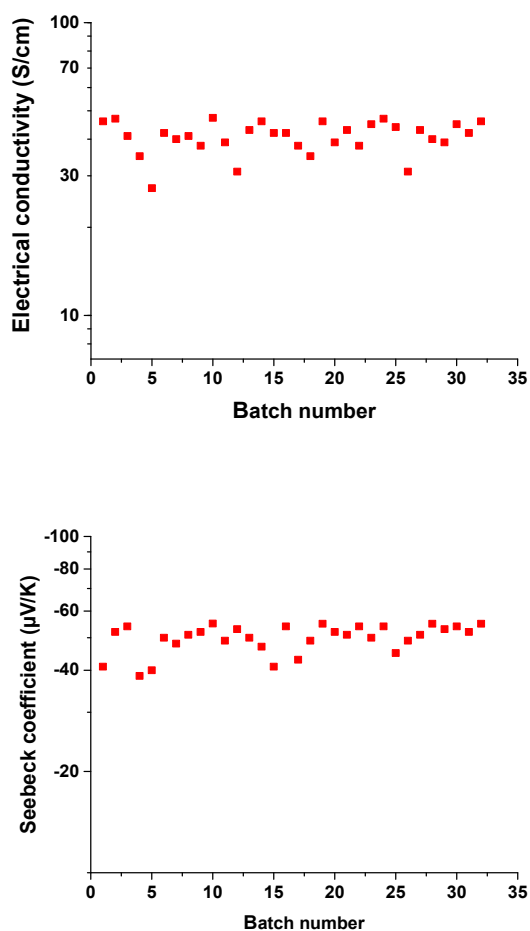


Fig. SA5. The electrical conductivity and the Seebeck coefficient of different batches for poly[Ni-tto] (P3, compressed pellets).

B) Simulation Data

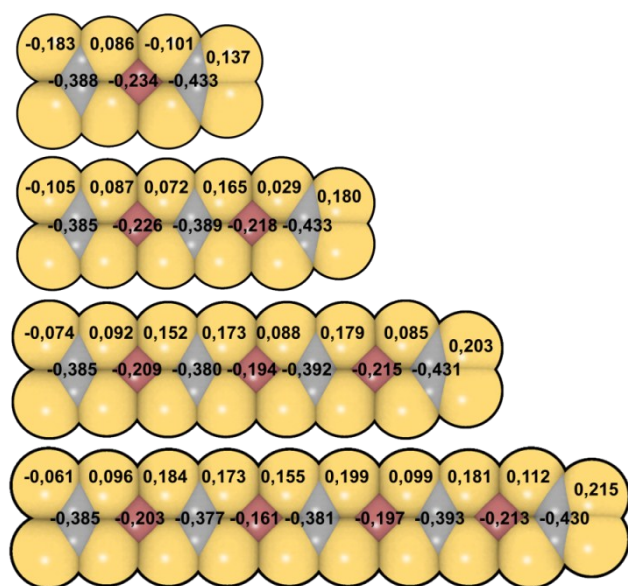


Fig. SB1 NBO charges^[1] of dianions of poly[Ni-tto] in NMF. The most negatively charged regions of the dianions are located at one chain end (left hand side) and atop of the CCNi centroid at another chain end (right hand side). Since the molecules are symmetric (mirror symmetry with respect to the horizontal axis), the charges are shown only for top side of the molecule for clarity. The dipole moments increase going from 10.5 D (one unit), 17.7 D (two units), 23.9 (three units) and 28.7 D (four units). The carbon, sulphur, nickel are shown as CPK spheres in grey, yellow, red, respectively.

Table SB1. Calculated average bond lengths (ℓ in Å), valent angles (θ , degrees) and dihedrals (φ , degrees) for the poly[Ni-tto] dianions in gas phase and in NMF.

Object/Medium	$\langle \ell_{\text{Ni-S}} \rangle$	$\langle \ell_{\text{S-C}} \rangle$	$\langle \ell_{\text{C-C}} \rangle$	$\langle \ell_{\text{S-C}} \rangle$ (terminal)	$\langle \theta_{\text{SNiS}} \rangle$	$\langle \theta_{\text{NiSC}} \rangle$	$\langle \varphi_{\text{SNISS}} \rangle$ (planarity)
one unit/gas	2.222± 0.051	1.702± 0.041	1.468	1.707± 0.061	91.9	103.0± 4.1	0.31
one unit/NMF	2.232± 0.034	1.733± 0.005	1.427	1.745± 0.062	91.9	103.1± 5.5	0.07
two units/gas	2.229± 0.016	1.719± 0.014	1.507± 0.016	1.666 (exact)	89.7± 0.2	106.8± 1.3	0.0
two units/NMF	2.153± 0.016	1.724± 0.004	1.441± 0.062	1.733± 0.014	91.4± 2.1	104.0± 3.6	0.0
three units/gas	2.218± 0.019	1.714± 0.016	1.498± 0.020	1.662 (exact)	90.0± 0.3	106.2± 1.3	0.0
three units/NMF	2.212± 0.013	1.716± 0.010	1.449± 0.053	1.728± 0.062	91.2± 1.7	104.3± 2.9	0.0
four units/gas	2.217± 0.018	1.712± 0.017	1.489± 0.019	1.659 (exact)	90.3± 0.3	105.9± 1.2	0.0
four units/NMF	2.215± 0.014	1.712± 0.011	1.453± 0.047	1.726± 0.062	91.1± 1.5	104.5± 2.5	0.0

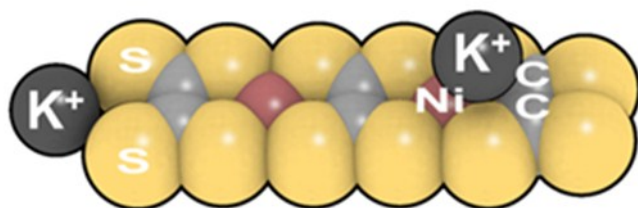


Fig. SB2 The K^+ positions of the poly[Ni-tto] chains. The structural model with two (Ni-tto) units is a representative example. The structure shown here represents the optimized geometry in NMF obtained in DFT calculations. The carbon, sulphur, nickel and potassium are shown as CPK spheres in grey, yellow, red and black, respectively.

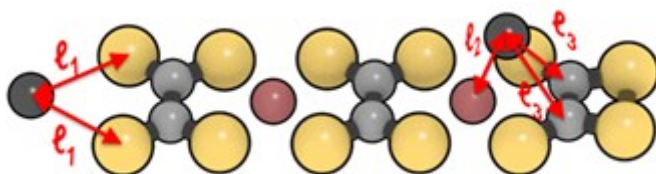


Fig. SB3 Defined distances between the atoms in poly[Ni-tto]. The structure shown here represents the optimized geometry in NMF obtained in DFT calculations. The distances are: $l_1=3.34\text{\AA}$, $l_2=3.61\text{\AA}$ and $l_3=3.82\text{\AA}$. The carbon, sulphur, nickel and potassium are shown as CPK spheres in grey, yellow, red and black, respectively.

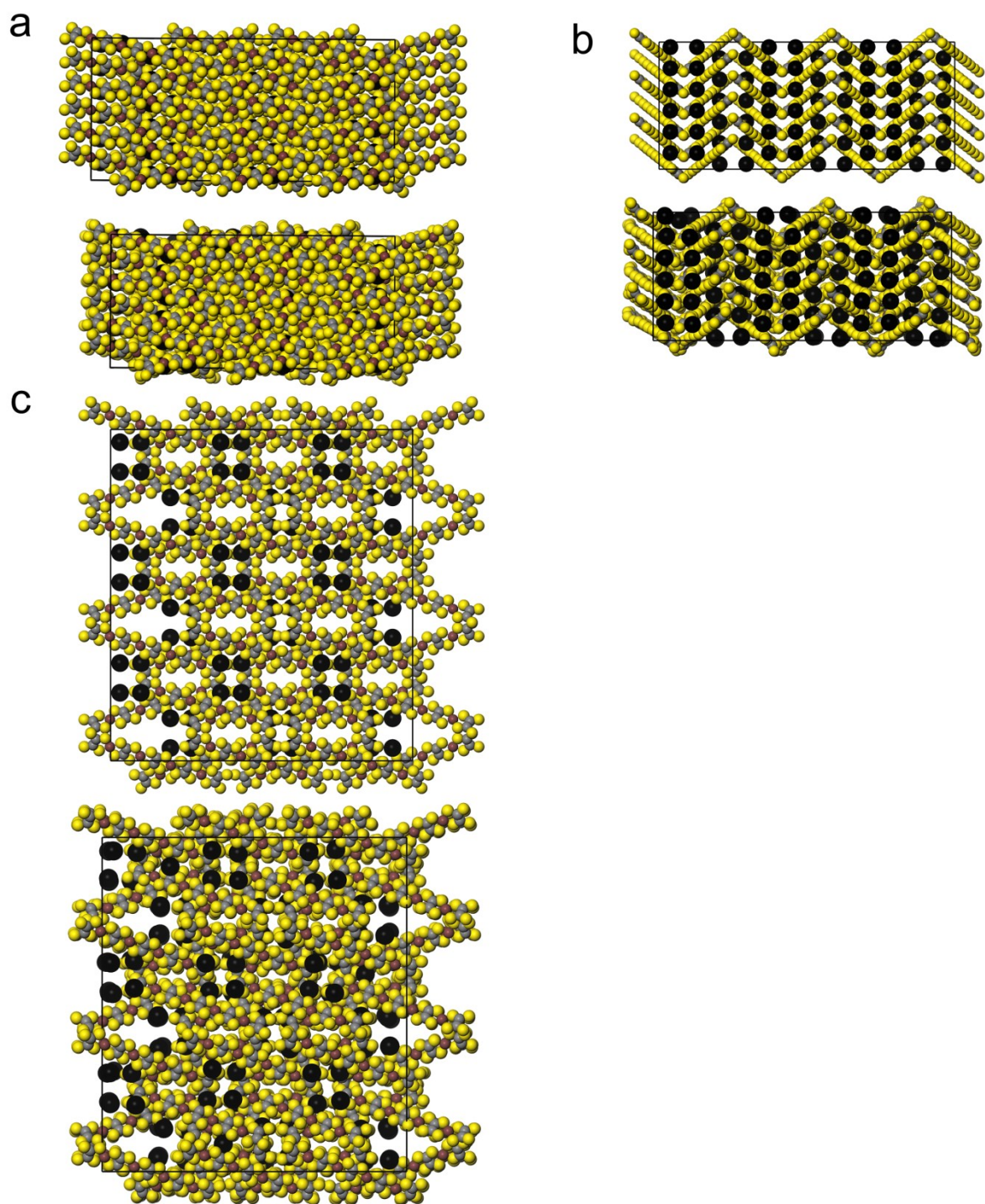


Fig. SB4 NVT-MD simulated supercell of poly[Ni-tto]. For each projection a, b and c, the initial and the final snap-shots (3-ns run) are shown. For the construction of the supercell, the predicted unit cell (Figure 2a, main text) was multiplied thrice along each coordinate vector.

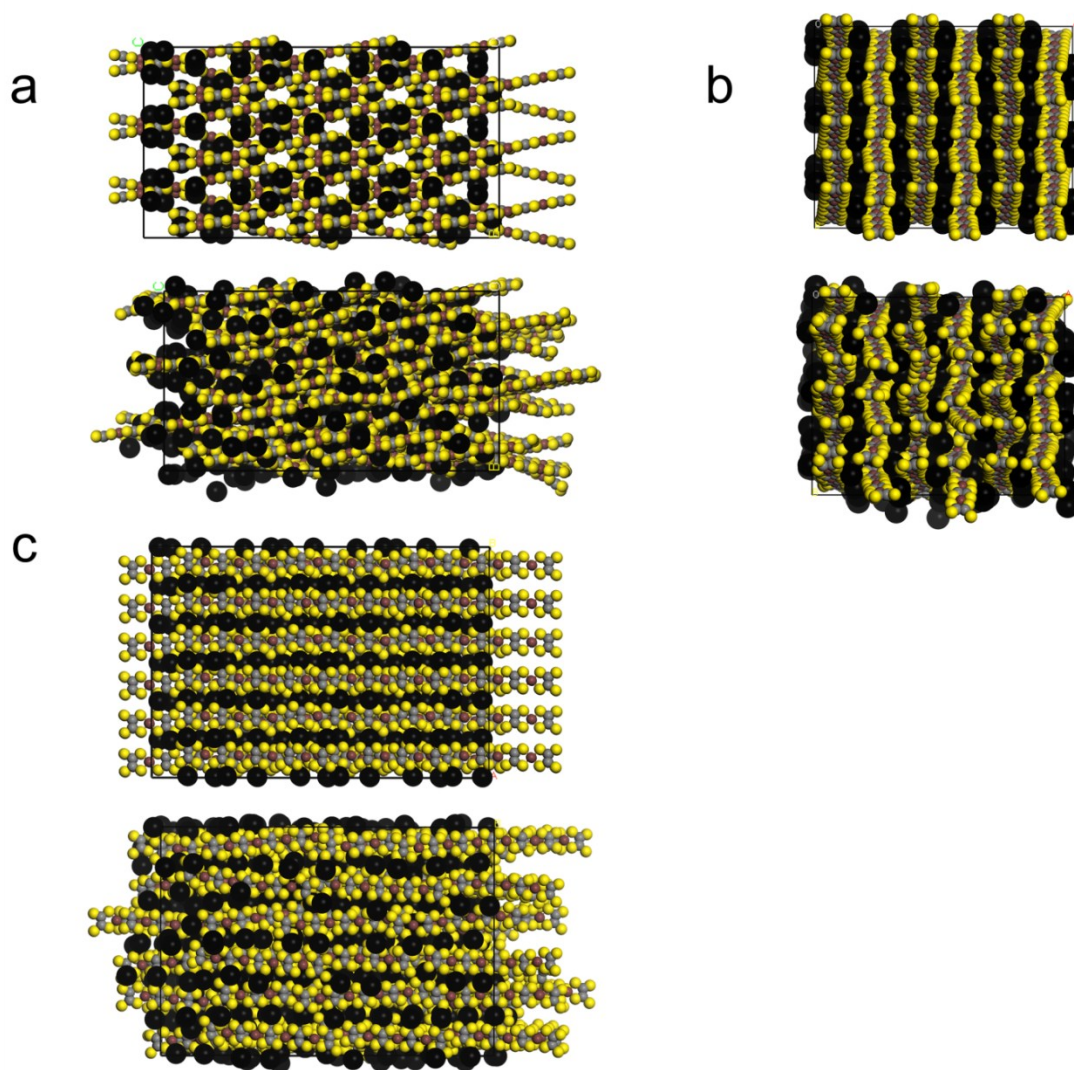


Fig. SB5 NVT-MD simulated supercell of $\text{poly}[\text{K}_x(\text{Ni-ett})]$. For each projection *a*, *b* and *c*, the initial and the final snap-shots (3-ns run) are shown. For the construction of the supercell, the predicted unit cell (Figure 2b, main text) was multiplied thrice along each coordinate vector.

Structural models from DFT calculations. For DFT calculations, the following structures have been selected: $\text{Ni}(\text{dmid})_2^{2-}$ and the models of both polymers 1-4 units in length, where the term “unit” refers to the number of Ni(II) coordinated with four S atoms (see **Experimental** in the main text). As an assumption in the calculations, $\text{poly}[\text{K}_x(\text{Ni-ett})]$ and $\text{poly}[\text{Ni-tto}]$ polymers differ in the number of K^+ cations.

At the beginning, the dianions of various lengths were optimized (1-4 units in length). Their geometrical metrics and the NBO analysis are presented in Supporting Information in **Table SB1** and **Figure SB1**. The polymer backbones are essentially planar independently on the solvent environment and the chain length. The calculated average bond length $\ell_{\text{Ni-S}}$ is in the range of 2.153-2.229Å, which agrees well with the results of simulations of nickel-bis-1,2-dithiolate dianions^[2] and the crystallographic data^[3]. The calculated lengths $\ell_{\text{Ni-S}}$ are slightly larger as compared to other experimental values of 2.13 - 2.17Å^[4,5]. However, as discussed previously^[4,6] this slight overestimation of the Ni-S bonds is typical for the DFT calculations. At the

same time, the lengths of the bonds (ℓ_{S-C} lengths close to double bonds and ℓ_{C-C} lengths are in-between the ordinary and double bonds) and the valent angles (θ) in the ligands are reproduced accurately by the calculations.^[3,6–10] Once the polymer units are immersed in highly polar NMF, the redistribution of the electronic density leads to the changes in the geometry and the dipole moments of dianions.

The NBO analysis (NBO stands for “natural bond orbital” analysis)^[1] (**Figure SB1**) reveals the most negatively charged regions of the polymer units, which are located at one end of the chain, and atop of the CCNi centroid at another chain end. These regions have been selected as an initial guess for the K^+ positions with interatomic distances exceeding 3.12 Å.^[11] Two counterions were added to poly[Ni-tto] and three-four to poly[K_x (Ni-ett)], depending on the chain length. The geometry optimizations of the complexes for poly[Ni-tto] show similar $\ell_1(K^+ \cdots S)$, $\ell_2(K^+ \cdots Ni)$, and $\ell_3(K^+ \cdots C)$ distances regardless the chain length. In **Figure SB3**, these distances are depicted for poly[Ni-tto] consisting of two units. This model of poly[Ni-tto] is further used in simulations.

For poly[K_x (Ni-ett)] chains with four units, the initial guess about the coordination positions of additional K^+ cations is less obvious. For example, the coordination was shown to happen on both sides of the Ni-dithiolate complexes, with K^+ cations being in the same plane of the square-planar complex,^[12,13] above and below the plane,^[11] or for instance, larger cations can build interlayers within [Ni(dmit)₂] sheets.^[14] Since the study of a complete potential energy surface for K^+ cations around poly[K_x (Ni-ett)] chains is impossible, the following assumptions were made: The K^+ cations were placed above and above and below the polymer backbone or were placed in the same plane of Ni complex (see **Experimental** in the main text). In first two cases, the backbones are found to be non-planar, and their energies are higher by ca. 10 kcal/mol as compared to the energy of the latter one. The $K^+ \cdots S$ distances in the complexes which K^+ placed in the same plane of Ni complex are the same as $\ell_1(K^+ \cdots S)$ from **Figure SB3**. This model of poly[K_x (Ni-ett)] is further used in simulations.

The predicted planarity of the polymer units contributes to insolubility of the polymers and to the formation of aggregates, as mentioned above. Besides, the close contacts of the charged planar polymer fragments and the counterions can cause the coupling of the units giving, for instance, various layered structures and nanosheets^[15] or 3D ordered packings.^[14]

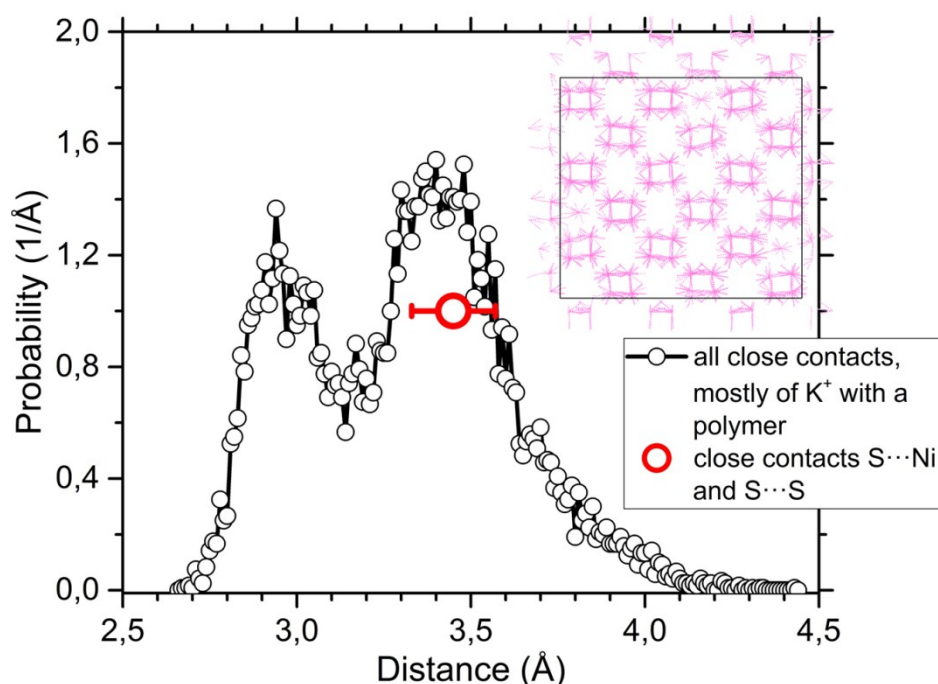


Fig. SB6A The analysis of the close contacts $S\cdots Ni$, $S\cdots S$ and the contacts of K^+ cations with poly[Ni-tto] **P3** during the 3-ns run. The close contacts as dashed magenta lines are shown in the insert, atoms are omitted for clarity. The average distance of the close contacts $S\cdots Ni$, $S\cdots S$ is $3.45 \pm 0.18 \text{ \AA}$. The distribution function showing all close contacts is bimodal with the most probable distances at 2.95 and 3.45 Å.

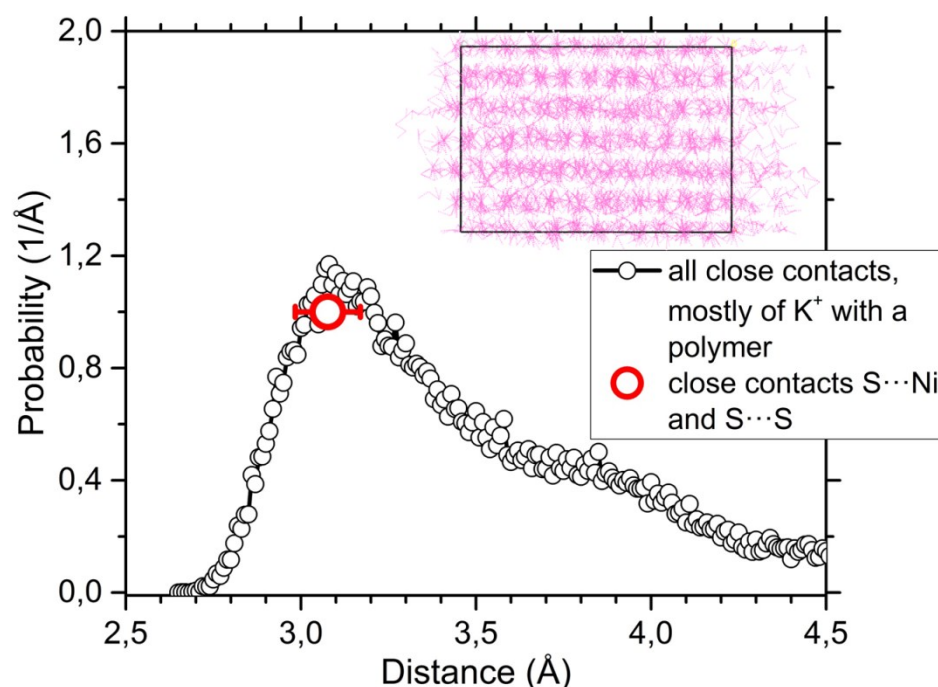


Fig. SB6B The analysis of the close contacts $S\cdots Ni$, $S\cdots S$ and the contacts of K^+ cations with poly[K_x(Ni-ett)] **P1** during the 3-ns run. The close contacts as dashed magenta lines are shown in the insert, atoms are omitted for clarity. The average distance of the close contacts $S\cdots Ni$, $S\cdots S$ is $3.08 \pm 0.09 \text{ \AA}$; it coincides with the contact distances of K^+ cations with all other atoms.

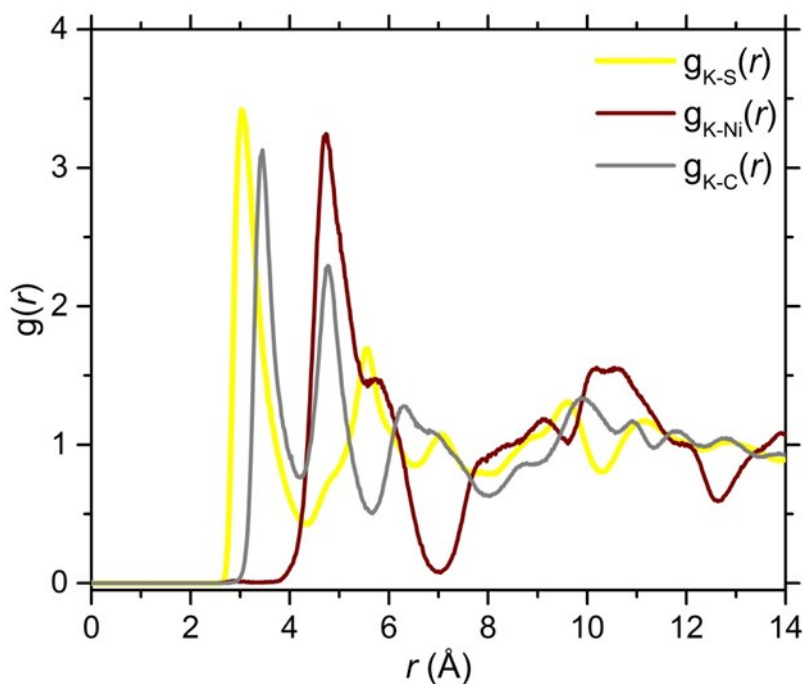


Fig. SB7A The radial distribution functions $g(r)$ for K and S atoms (yellow curve, the first peak is at 3.05 Å, the second at 5.53 Å), K and Ni (dark red curve, the first two peaks are located at 4.73 and 5.73 Å, the second peak is at 9.09 Å) and K and C (grey curve, the first and the second peaks are at 3.45 and 4.37 Å) in poly[Ni-tto].

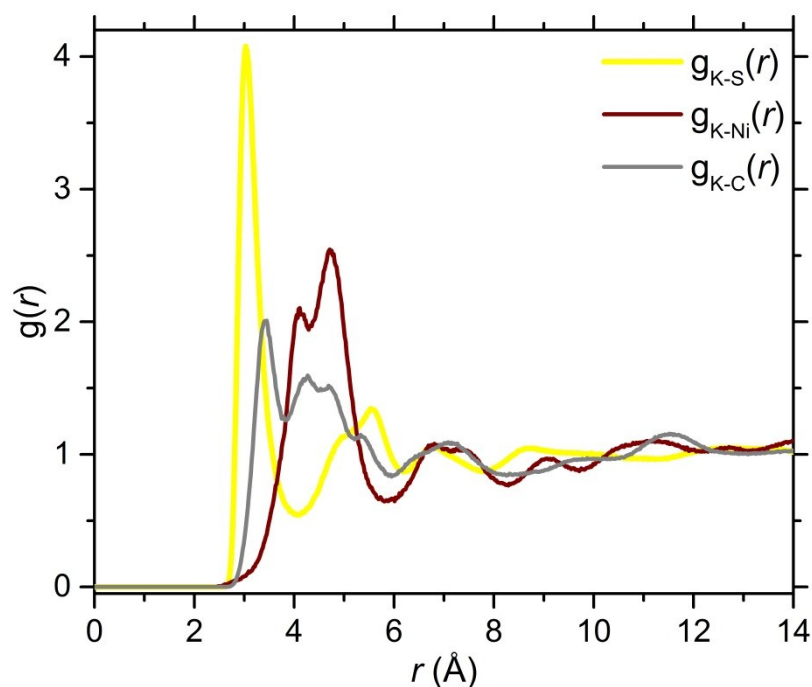


Fig. SB7B The radial distribution functions $g(r)$ for K and S atoms (yellow curve, the first peak is at 3.03 Å, the second at 5.53 Å), K and Ni (dark red curve, the first peak is located at 4.11, the second peak is at 4.71 Å) and K and C (grey curve, the first peak is at 3.41 and the second is at 4.27 Å) in poly[K_x(Ni-ett)].

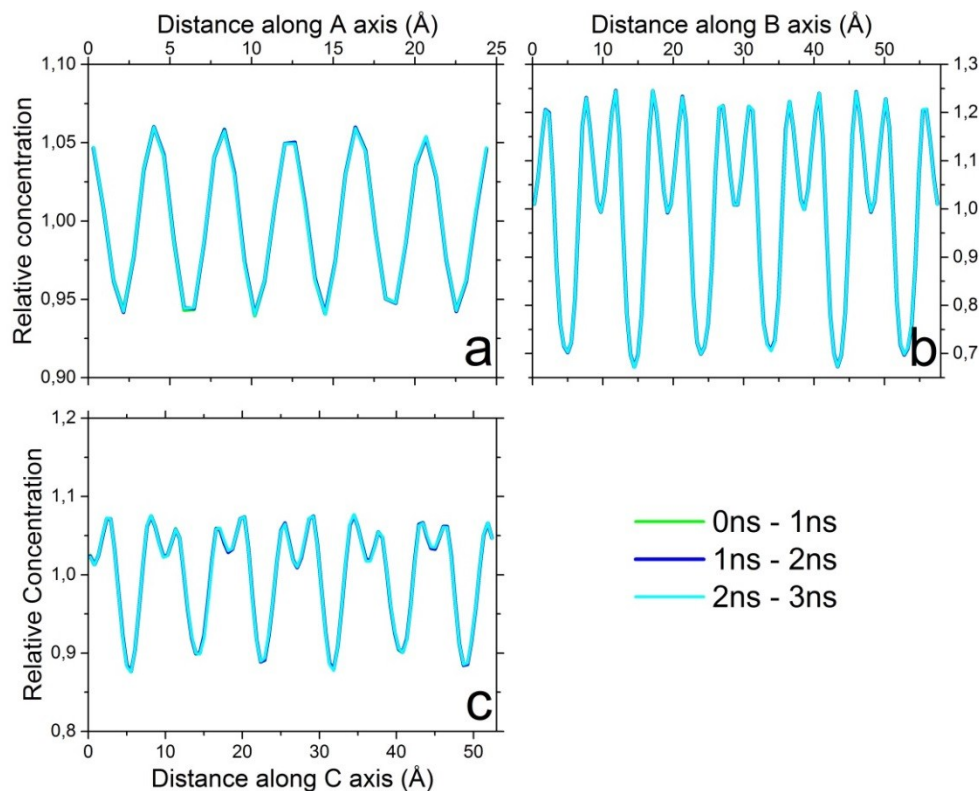


Fig. SB8A The smoothed averaged concentration profiles along the A (a), B (b) and C (c) axes of the supercell of poly[Ni-tto] **P3** for different parts of the MD trajectory.

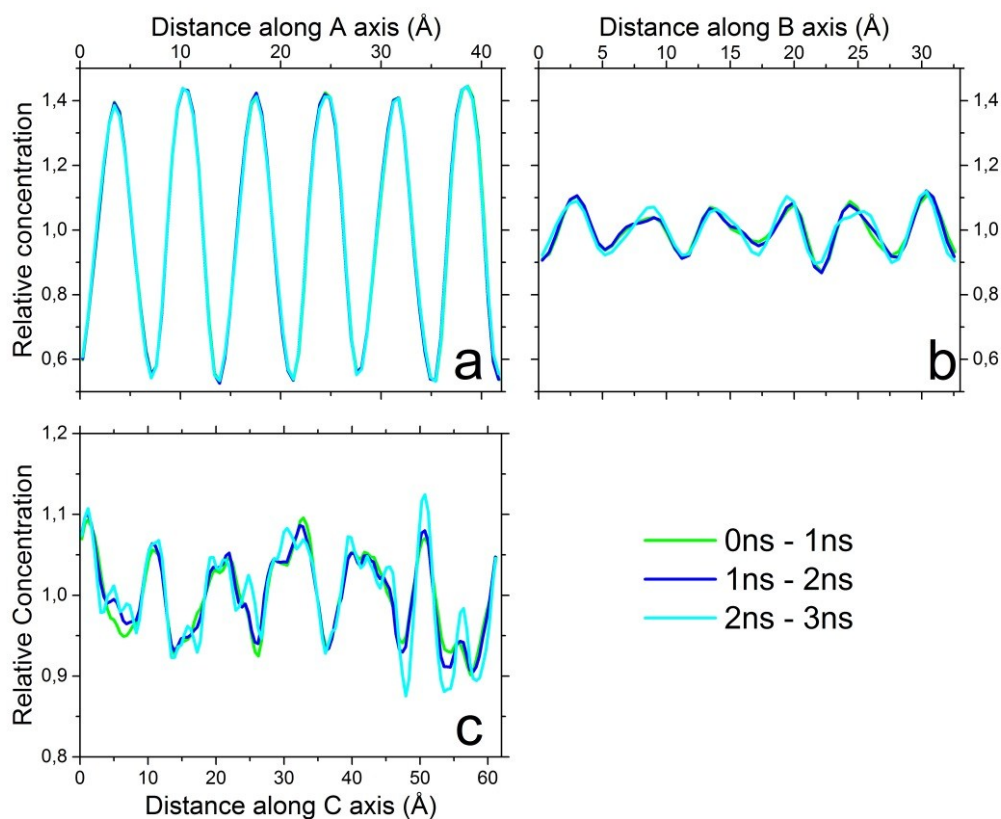


Fig. SB8B The smoothed averaged concentration profiles along the A (a), B (b) and C (c) axes of the supercell of poly[K_x(Ni-ett)] **P1** for different parts of the MD trajectory.

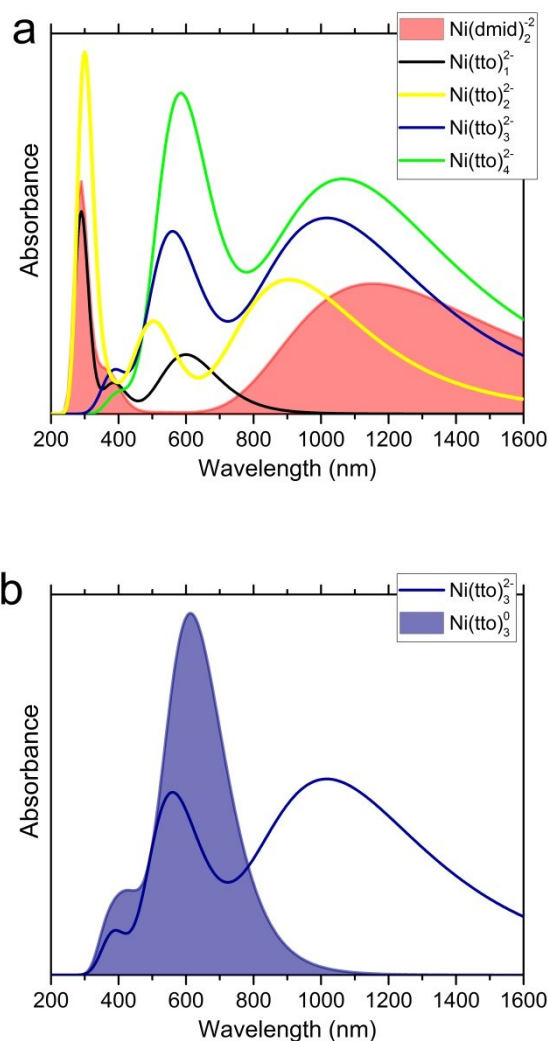


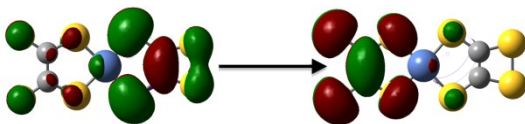
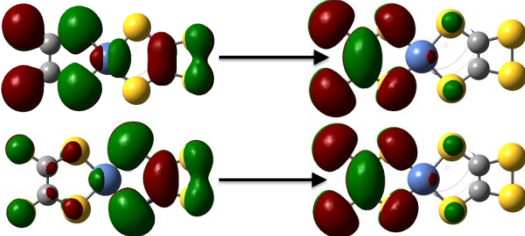
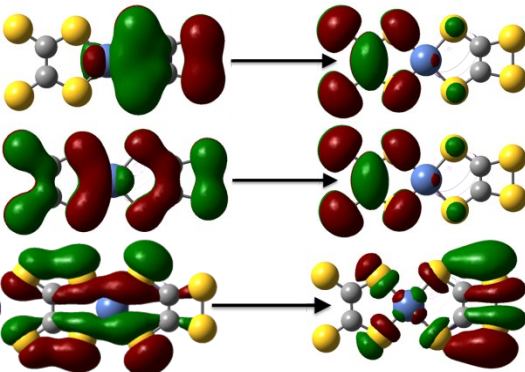
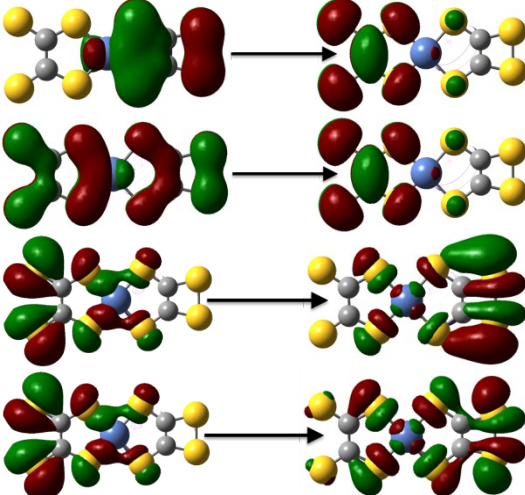
Fig. SB9 (a) calculated UV-Vis spectra for Ni(dmid)_2^{2-} as well as dianions of poly[Ni-tto] in NMF depending on the number of the units and (b) calculated UV-Vis spectra for $(\text{Ni-tto})_3^{2-}$ and neutral complex of the same length in NMF.

The electronic transition involves the electron transfer from one dithiolene ligand to the other one. Indeed, the TD-DFT calculations (**Figure SB9a**) of Ni(dmid)_2^{2-} complex confirm the band at this spectral region corresponds to the electron transfer from one ligand to another one. It is depicted as well in **Table SB2** for poly[Ni-tto] dianions of different lengths.

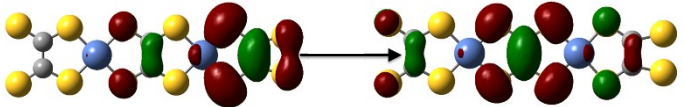
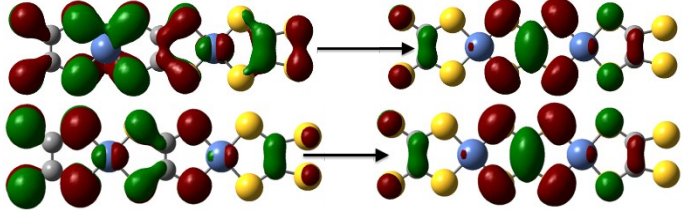
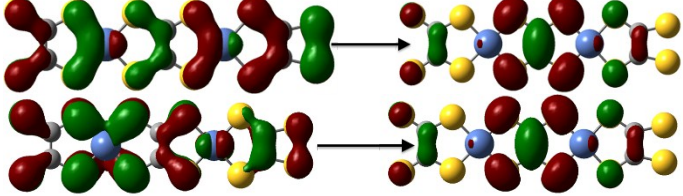
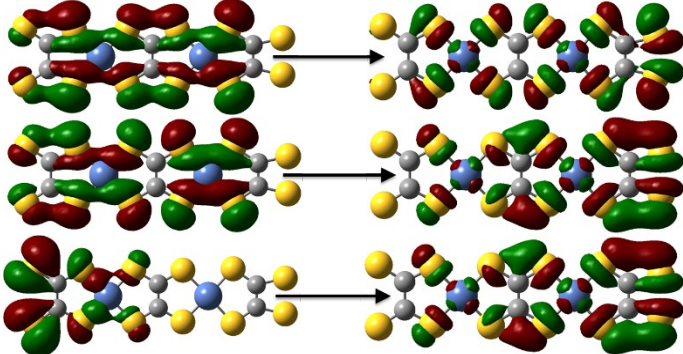
In accordance to experimental data, the intense low-energy transitions vanish for the neutral poly[Ni-tto] chain as seen in calculated electronic spectrum (**Figure SB9b**). These results are in agreement with earlier studies of neutral and charged Ni complexes by Schrauzer and Mayweg^[16] and in other investigations.^[17]

Table SB2. Vertical electronic transitions for the oscillator strengths $f > 0.1$, shapes of the involved orbitals, the electronic energies for poly[Ni-tto] dianions in NMF (see Figure SB9).

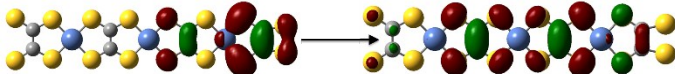
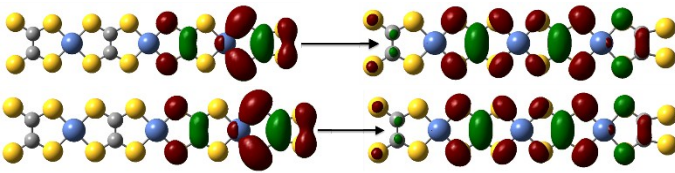
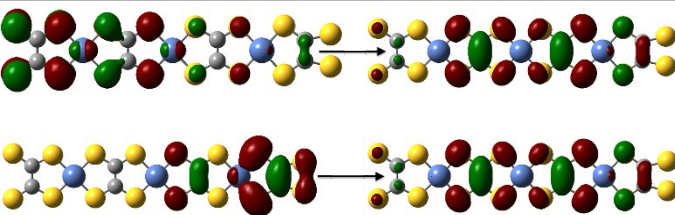
A. (Ni-tto)²⁻₁

Electronic transition	Key excitations (coefficient)	Shape of the involved molecular orbitals (104-HOMO, 105-LUMO)	Electronic energies E [eV] and wave length λ [nm]	Oscillator strength f
$S_0 \rightarrow S_5$	104 \rightarrow 105 (0.69)		2.0860 / 594	0.2432
$S_0 \rightarrow S_{13}$	100 \rightarrow 105 (0.67) 104 \rightarrow 105 (0.14)		3.1961 / 387	0.1214
$S_0 \rightarrow S_{20}$	90 \rightarrow 105 (0.25) 94 \rightarrow 105 (0.57) 97 \rightarrow 106 (0.12)		4.1964 / 295	0.3202
$S_0 \rightarrow S_{22}$	90 \rightarrow 105 (0.12) 94 \rightarrow 105 (0.24) 102 \rightarrow 106 (0.46) 102 \rightarrow 107 (0.33)		4.4385 / 279	0.4386

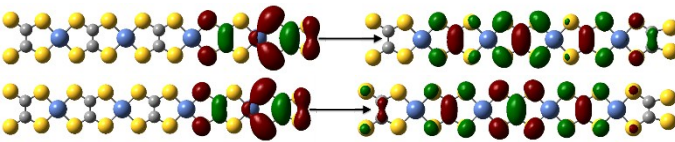
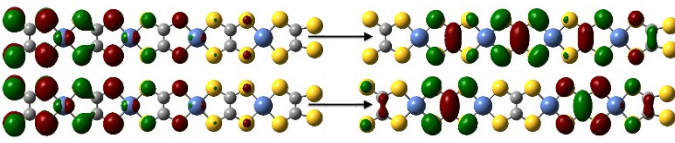
B. (Ni-tto)²⁻₂

Electronic transition	Key excitation (coefficient)	Shape of the involved molecular orbitals (133-HOMO, 134-LUMO)	Electronic energies E [eV] and wave length λ [nm]	Oscillator strength f
$S_0 \rightarrow S_1$	133 \rightarrow 134 (0.69)		1.3695 / 905	0.5225
$S_0 \rightarrow S_{13}$	125 \rightarrow 134 (0.14) 129 \rightarrow 134 (0.67)		2.4368 / 509	0.3228
$S_0 \rightarrow S_{36}$	117 \rightarrow 134 (0.48) 125 \rightarrow 134 (0.23)		3.9102 / 317	0.3913
$S_0 \rightarrow S_{42}$	120 \rightarrow 138 (0.11) 123 \rightarrow 136 (0.22) 132 \rightarrow 136 (0.30)		4.1742 / 297	0.9772

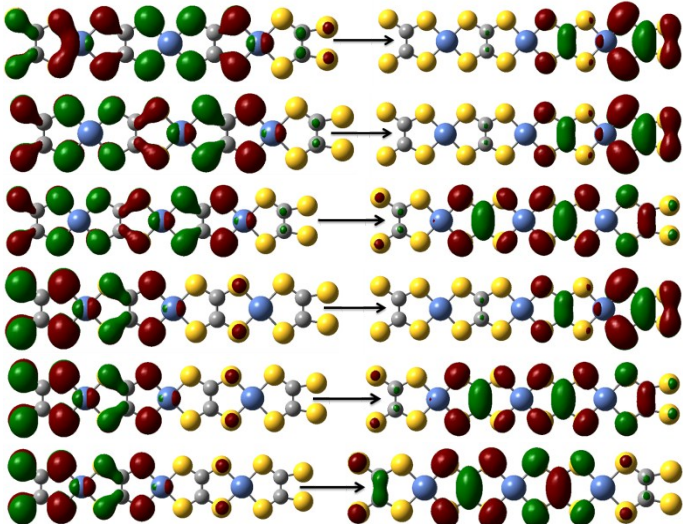
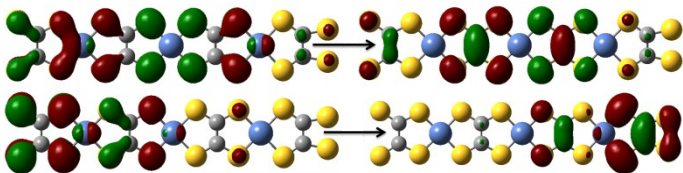
C. (Ni-tto)²⁻₃

Electronic transition	Key excitation (coefficient)	Shape of the involved molecular orbitals (180-HOMO, 181-LUMO)	Electronic energies <i>E</i> [eV] and wave length λ [nm]	Oscillator strength <i>f</i>
S ₀ →S ₁	180→181 (0.64)		1.2143 / 1021	0.7585
S ₀ →S ₁₂	180→181 (0.22) 180→182 (0.58)		2.0121 / 616	0.2181
S ₀ →S ₁₇	177→181 (0.55) 180→182 (0.23)		2.2758 / 544	0.5385

D. (Ni-tto)²⁻₄

Electronic transition	Key excitation (coefficient)	Shape of the involved molecular orbitals (227-HOMO, 228-LUMO)	Electronic energies <i>E</i> [eV] and wave length λ [nm]	Oscillator strength <i>f</i>
S ₀ →S ₁	227→228 (0.57) 227→230 (0.15)		1.1544 / 1074	0.9027
S ₀ →S ₂₀	224→228 (0.53) 224→229 (0.30)		2.1363 / 580	1.1498

E. (Ni-tto)⁰₃

Electronic transition	Key excitation (coefficient)	Shape of the involved molecular orbitals (179-HOMO, 180-LUMO)	Electronic energies <i>E</i> [eV] and wave length λ [nm]	Oscillator strength <i>f</i>
$S_0 \rightarrow S_{13}$	168 \rightarrow 180 (0.11) 173 \rightarrow 180 (0.30) 173 \rightarrow 181 (0.13) 177 \rightarrow 180 (0.40) 177 \rightarrow 181 (0.40) 177 \rightarrow 182 (0.16)		2.0172 / 614	1.3860
$S_0 \rightarrow S_{33}$	168 \rightarrow 182 (0.12) 177 \rightarrow 180 (0.48)		2.8219 / 439	0.1861

C) XPS data

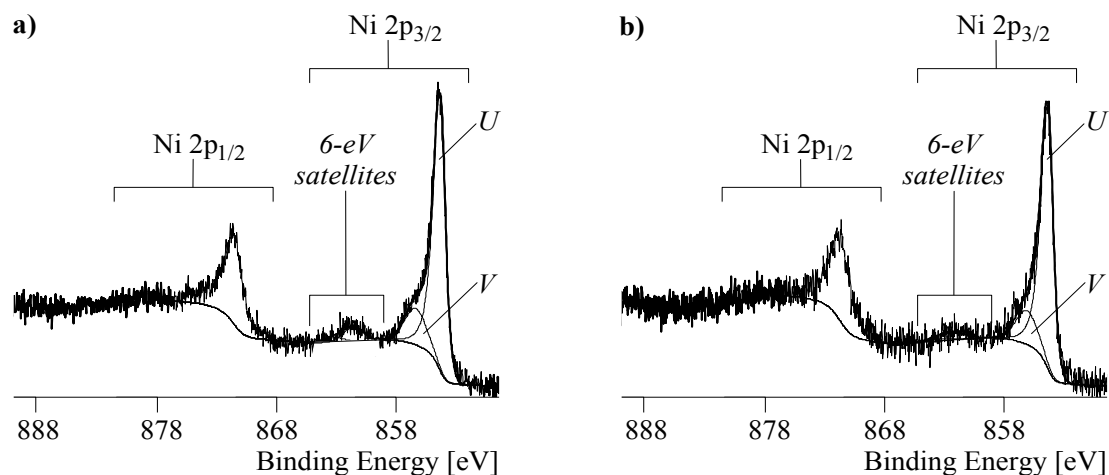
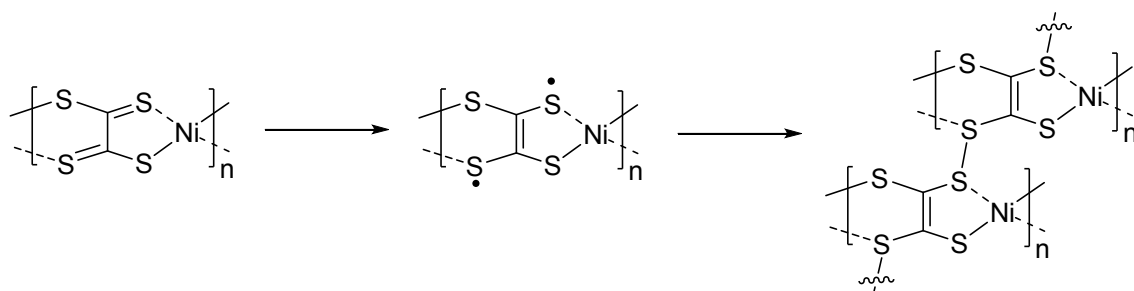


Figure SC1. XPS high-resolution Ni 2p spectra and their deconvolutions for poly[K_x(Ni-ett)] (a) and poly[Ni-tto] (b) samples.

Due to the *spin-orbit-interaction* all Ni 2p spectra are composed of the Ni 2p_{3/2} and Ni 2p_{1/2} peaks (Figure SC1). In order to discuss the binding states of nickel, the Ni 2p_{3/2} spectra were deconvoluted into two component peaks. Component peaks U at 854.0 eV represented the nickel atoms in poly[K_x(Ni-ett)] and poly[Ni-tto]. The binding energy values found were slightly higher as given in literature for NiS and NiS₂. The origin of component peaks V (855.87 eV) was not very clear. The chemical shift observed and the increased width (compared to component peaks U) of these component peaks indicated the presence of differently oxidized nickel species on the surface of the samples. These findings corresponded to the partly oxidation of sulphur observed in the S 2p spectra. Thus, binding energy values of 855.2–856.8 eV were expected for nickel in NiSO₄. In addition, the Ni 2p spectra showed two so-called 6-eV *satellites*. In its initial state the electron configuration of the Ni is K²L⁸ 3s² 3p⁶ 3d⁹ 4s¹. If one electron is removed during the photoionization, the Ni atom can exist in the two final states [K²L⁸ 3s² 3p⁶]⁻¹ 3d¹⁰ 4s (corresponds to the ground state) and [K²L⁸ 3s² 3p⁶]⁻¹ 3d⁹ 4s² (two-hole configuration as excited state) having an energy difference of roughly 6 eV. The first electron configuration gave the component peaks (U and V) and the second one the two 6-eV *satellites*. Actually, for the 6-eV *satellites* shifts of about 7 eV were found.

As mentioned above, component peaks P (BE[S 2p_{3/2}] = 163.12 eV) could result from disulfides (⁻P_S-⁻P_S). It should be noted that the formation of disulfides did not require the presence of an oxidizing agent. After the homolytic cleavage of C=S bonds (**Scheme SC1**) disulfide bridges can be formed between the two polymer chains and, obviously, the presence of such intermolecular bonds is one of the factors causing the insolubility of the formed polymer.



Scheme SC1. Possible routes of disulfides formation

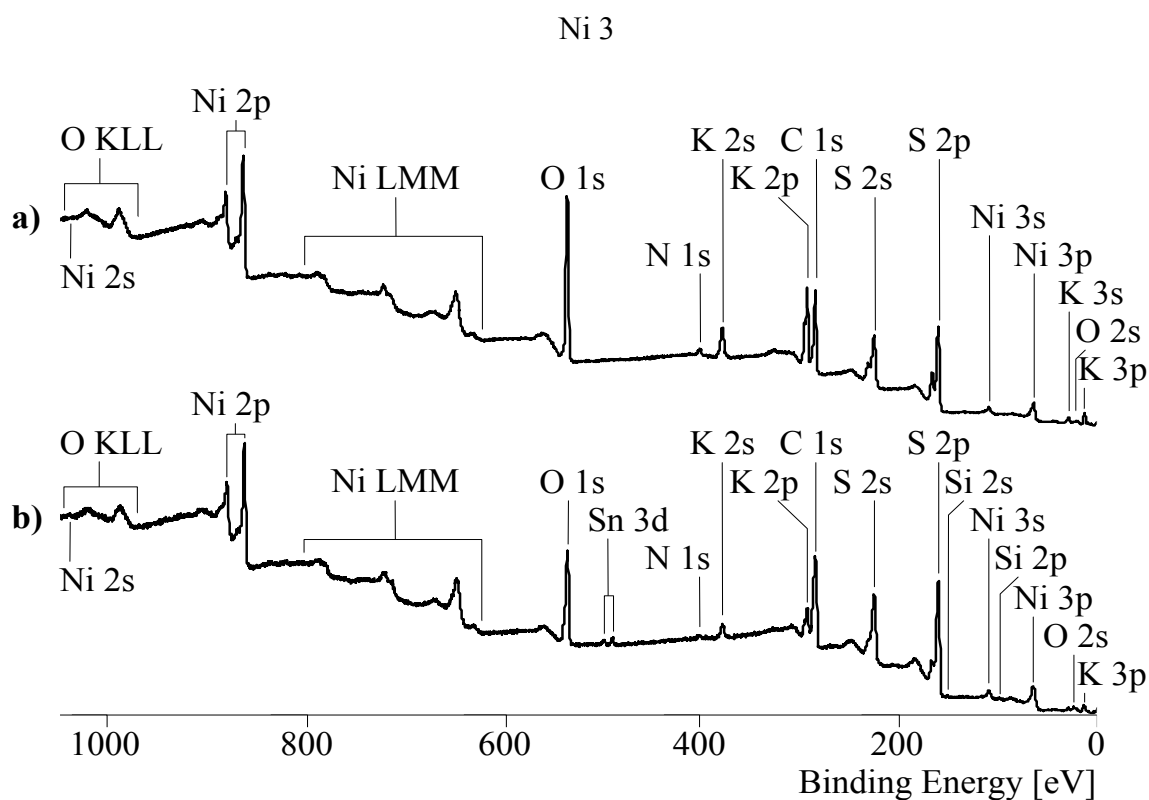


Figure SC2. XPS survey spectra for poly[K_x(Ni-ett)] (a) and poly[Ni-tto] (b) samples.

Table SC1. Relative compositions of the sample surfaces determined by means of XPS (all atomic ratios were related to carbon content)

	<i>poly[K_x(Ni-ett)]</i>	<i>poly[Ni-tto]</i>
[N]:[C]	0.042	0.013
[O]:[C]	0.424	0.250
[Si]:[C]	–	0.005
[S]:[C]	0.368	0.332
[K]:[C]	0.177	0.028
[Ni]:[C]	0.076	0.063

The increased carbon content is explained by the fact that the surface layer of the sample contains a significant amount of adsorbed impurities (hydrocarbons).

Table SC2. XPS deconvolution parameters of C 1s, S 2p, K 2p, and Ni 2p high-resolution XPS spectra of *poly[K_x(Ni-ett)]* sample

C 1s spectrum

Peak	Position BE (eV)	FWHM (eV)	Raw Area (CPS)	Height	Atomic Conc %	Mass Conc %
C 1s <i>S</i>	285.000	1.585	3563.3	2216	68.43	68.43
C 1s <i>B</i>	285.921	1.318	665.3	460	12.77	12.77
C 1s <i>C</i>	286.816	1.318	534.1	369	10.25	10.25
C 1s <i>D</i>	288.003	1.318	219.8	152	4.22	4.22
C 1s <i>E</i>	289.105	1.318	225.6	156	4.33	4.33

S 2p spectrum

Peak	Position BE (eV)	FWHM (eV)	Raw Area (CPS)	Height	Atomic Conc %	Mass Conc %
S 2p _{3/2} <i>O</i>	162.203	0.842	1387.9	1503	23.44	23.44
S 2p _{1/2} <i>O'</i>	163.384	0.842	693.9	752	23.44	23.44
S 2p _{3/2} <i>P</i>	163.122	1.166	581.5	454	9.82	9.82
S 2p _{1/2} <i>P'</i>	164.303	1.166	290.8	227	9.82	9.82
S 2p _{3/2} <i>Q</i>	164.049	1.143	386.4	308	6.53	6.53
S 2p _{1/2} <i>Q'</i>	165.230	1.143	193.2	154	6.53	6.53
S 2p _{3/2} <i>R</i>	168.869	1.041	605.6	530	10.21	10.21
S 2p _{1/2} <i>R'</i>	170.050	1.041	302.8	265	10.21	10.21

K 2p spectrum

Peak	Position BE (eV)	FWHM (eV)	Raw Area (CPS)	Height	Atomic Conc %	Mass Conc %
K 2p _{3/2}	293.142	1.304	3104.8	2346	49.65	49.65
K 2p _{1/2}	295.986	1.162	1575.1	1235	50.35	50.35

Ni 2p_{3/2} spectrum

Peak	Position BE (eV)	FWHM (eV)	Raw Area (CPS)	Height	Atomic Conc %	Mass Conc %
Ni 2p _{3/2} <i>U</i>	854.036	1.407	3953.5	2688	75.47	75.47
Ni 2p _{3/2} <i>V</i>	855.893	2.139	867.3	407	16.54	16.54
Ni 2p _{3/2} <i>SU</i>	861.491	2.022	182.2	104	6.56	6.56
Ni 2p _{3/2} <i>SV</i>	863.347	2.022	75.4	34	1.43	1.43

The abbreviations Ni 2p_{3/2} *SU* and Ni 2p_{3/2} *SV* show the parameters of the 6-eV *satellites* in the Ni 2p_{3/2} spectrum.

Table SC3. XPS deconvolution parameters of C 1s, S 2p, K 2p, and Ni 2p high-resolution XPS spectra of poly(Ni-tto) sample

C 1s spectrum

Peak	Position BE (eV)	FWHM (eV)	Raw Area (CPS)	Height	Atomic Conc %	Mass Conc %
C 1s <i>S</i>	285.000	1.598	1359.8	838	41.38	41.38
C 1s <i>B</i>	285.967	1.318	229.3	159	6.98	6.98
C 1s <i>C</i>	286.422	1.346	557.9	378	16.97	16.97
C 1s <i>D</i>	287.722	1.405	996.0	647	30.29	30.29
C 1s <i>E</i>	289.237	1.318	143.9	100	4.38	4.38

S 2p spectrum

Peak	Position BE (eV)	FWHM (eV)	Raw Area (CPS)	Height	Atomic Conc %	Mass Conc %
S 2p _{3/2} <i>O</i>	162.033	0.785	890.7		27.51	27.51
S 2p _{1/2} <i>O'</i>	163.214	0.785	445.4		27.50	27.50
S 2p _{3/2} <i>P</i>	163.123	1.342	411.1		12.69	12.69
S 2p _{1/2} <i>P'</i>	164.303	1.342	205.6		12.69	12.69
S 2p _{3/2} <i>Q</i>	163.967	1.346	211.9		6.55	6.55
S 2p _{1/2} <i>Q'</i>	165.148	1.346	106.2		6.55	6.55
S 2p _{3/2} <i>R</i>	168.926	1.212	105.6		3.26	3.26
S 2p _{1/2} <i>R'</i>	170.107	1.212	52.8		3.26	3.26

K 2p spectrum

Peak	Position BE (eV)	FWHM (eV)	Raw Area (CPS)	Height	Atomic Conc %	Mass Conc %
K 2p _{3/2}	292.944	1.230	317.7	254	49.67	49.67
K 2p _{1/2}	295.797	1.096	161.1	134	50.33	50.33

Ni 2p_{3/2} spectrum

Peak	Position BE (eV)	FWHM (eV)	Raw Area (CPS)	Height	Atomic Conc %	Mass Conc %
Ni 2p _{3/2} <i>U</i>	853.996	1.404	1992.6	1357	76.08	76.08
Ni 2p _{3/2} <i>V</i>	855.853	2.134	466.0	219	17.78	17.78
Ni 2p _{3/2} <i>SU</i>	861.690	2.334	130.4	51	4.96	4.96
Ni 2p _{3/2} <i>SV</i>	862.988	2.334	31.0	12	1.18	1.18

The abbreviations Ni 2p_{3/2} *SU* and Ni 2p_{3/2} *SV* show the parameters of the 6-eV *satellites* in the Ni 2p_{3/2} spectrum.

D) Thermogravimetric and elemental analysis

The TGA curves for both poly[K_x(Ni-ett)] and poly[Ni-tto] samples are shown in **Figure SD1**. Both samples show an initial 2.5 % weight loss for two isothermal holds at 50 °C and 100 °C. After next isothermal holds by 200 °C the rest of poly[Ni-tto] is 95 %, while only 92 % by poly[K_x(Ni-ett)]. More thermally stable poly[Ni-tto] sample indicating the absence of additional functionalities, which making product less stable.

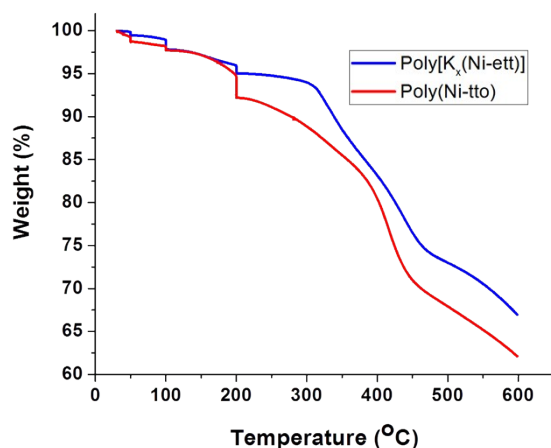
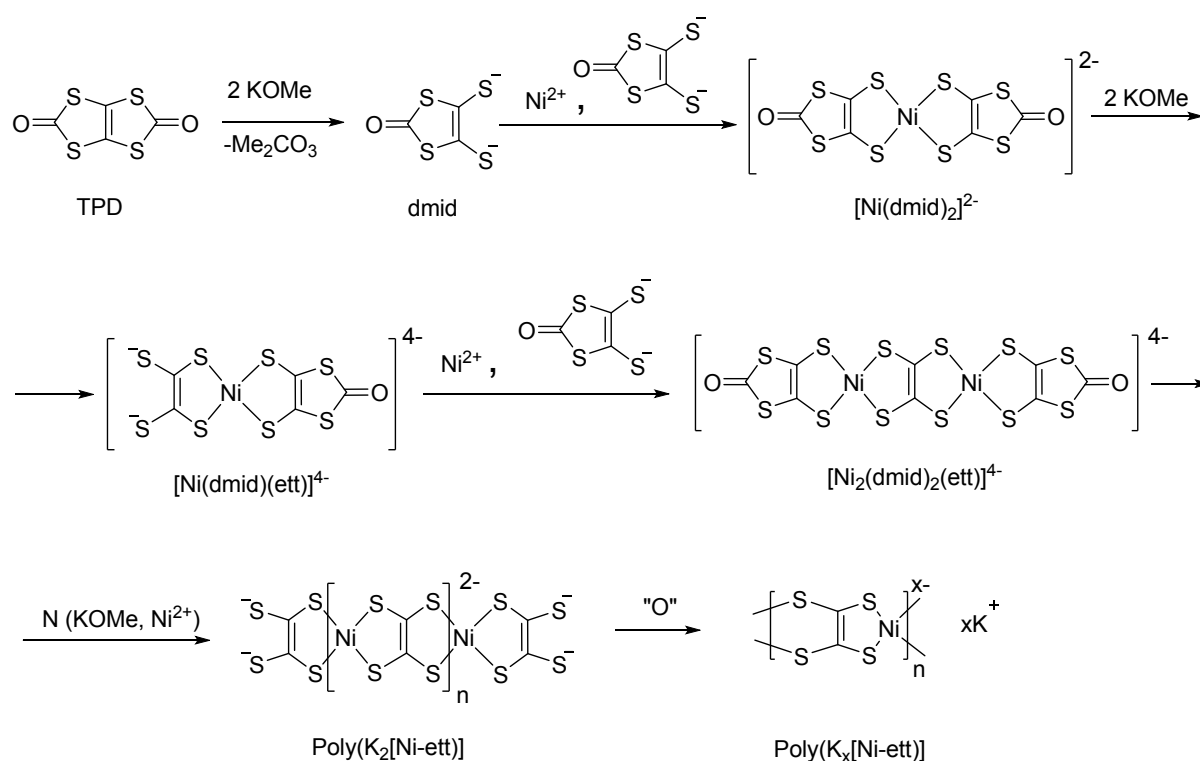


Figure SD1. TGA analysis, weight % vs. temperature for the poly[K_x(Ni-ett)] and poly[Ni-tto] samples.

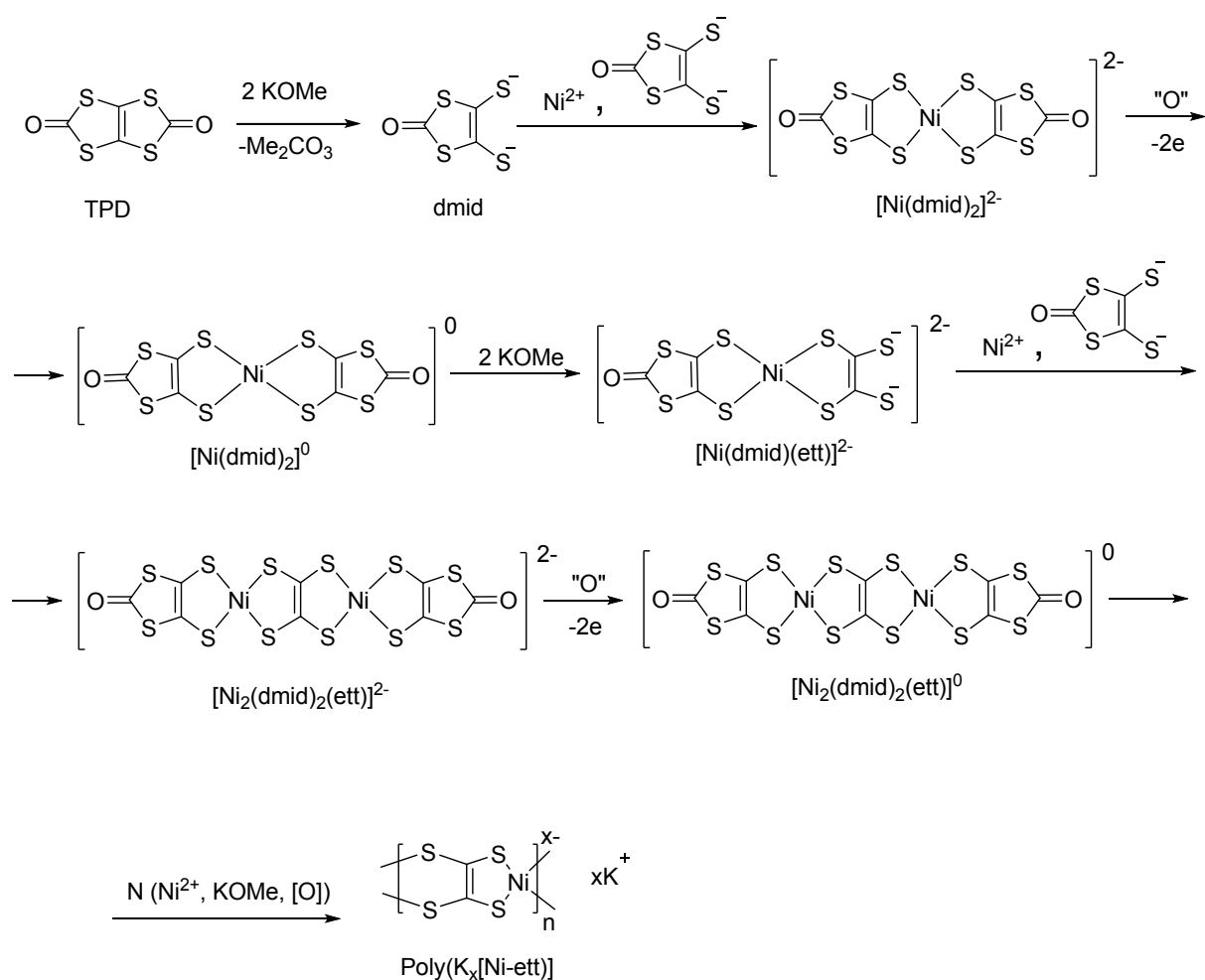
	K	Ni	S	C	H
poly[K _x (Ni-ett)] (P1 _{Methanol})	3,59	21,17	41,53	12,46	1,13
poly[K _x (Ni-ett)] (P2)	12,59	22,98	53,18	9,88	0,76
poly[K _x (Ni-ett)] (P2-ox)	0,96	13,67	39,92	9,23	1,18

Table SD1. Elemental composition of **P1**_{Methanol}, **P2** and **P2-ox** polymers (weight %). The presence of hydrogen may be attributed to water molecules, which are strongly coordinated with polymer and cannot be completely removed. For **P1**_{Methanol} and **P2-ox** the summing of element weights are much lower 100%. The remainder we assume as oxygen.

E) Scheme of tentative polymerization mechanism



Scheme SE1. Tentative polymerization mechanism under non-oxidative conditions (P2). The last step shows the “post-polymerization” oxidation by the air oxygen during washing of the polymer in open atmosphere.



Scheme SE2. Tentative oxidation-induced formation of longer polymer chains during washing of the polymer in open atmosphere.

References

- [1] E. D. Glendening, A. E. Reed, J. E. Carpenter, F. Weinhold, *NBO Version 3.1*.
- [2] A. Zarkadoulas, M. J. Field, V. Artero, C. A. Mitsopoulou, *ChemCatChem* **2017**, *9*, 2308.
- [3] S.-G. Liu, Y.-Q. Liu, Y.-F. Li, D.-B. Zhu, *Synth. Met.* **2000**, *114*, 139.
- [4] Q. Yu, J.-Y. Ge, Z.-P. Lv, H.-Y. Wang, J.-L. Zuo, *RSC Adv* **2016**, *6*, 100783.
- [5] L. Qu, Y. Guo, H. Luo, C. Zhong, G. Yu, Y. Liu, J. Qin, *Chem. Commun. (Cambridge, England)* **2012**, *48*, 9965.
- [6] K. Ray, T. Weyhermüller, F. Neese, K. Wieghardt, *Inorg. Chem.* **2005**, *44*, 5345.
- [7] D. Belo, M. J. Figueira, J. P. M. Nunes, I. C. Santos, L. C. Pereira, V. Gama, M. Almeida, C. Rovira, *J. Mater. Chem.* **2006**, *16*, 2746.
- [8] C. M. Amb, C. L. Heth, S. J. Evenson, K. I. Pokhodnya, S. C. Rasmussen, *Inorg. Chem.* **2016**, *55*, 10978.
- [9] G. Soras, N. Psaroudakis, M. J. Manos, A. J. Tasiopoulos, D. G. Liakos, G. A. Mousdis, *Polyhedron* **2013**, *62*, 208.
- [10] T. Vogt, C. Faulmann, R. Soules, P. Lecante, A. Mosset, P. Castan, P. Cassoux, J. Galy, *J. Am. Chem. Soc.* **1988**, *110*, 1833.
- [11] C. C. Kirkpatrick, J. N. Truong, B. A. Kowert, *J. Comput. Chem.* **2017**, *38*, 93.
- [12] E. Delgado, C. J. Gómez-García, D. Hernández, E. Hernández, A. Martín, F. Zamora, *Dalton Trans. (Cambridge, England 2003)* **2016**, *45*, 6696D..
- [13] Tiana, C. H. Hendon, A. Walsh, T. P. Vaid, *Phys. Chem. Chem. Phys.* **2014**, *16*, 14463.
- [14] H. Yang, D.-Y. An, J.-L. Liu, X.-M. Ren, L.-C. Zhou, H.-B. Wang, *RSC Adv.* **2015**, *5*, 13857.
- [15] H. Maeda, R. Sakamoto, H. Nishihara, *Langmuir* **2016**, *32*, 2527.
- [16] G. N. Schrauzer, V. P. Mayweg, *J. Am. Chem. Soc.* **1965**, *87*, 3585.
- [17] P. Deplano, M. L. Mercuri, A. Serpe, L. Pilia (Ed.), *PATAI'S Chemistry of Functional Groups: Structure and Properties of d8 Metal-Dithiolene Complexes* **2010**.